

Multi-Kernel Filtering: An Extension of Bilateral Filtering Using Image Context[★]

Feihong Liu^{a,b}, Jun Feng^{a,*}, Pew-Thian Yap^{b,*} and Dinggang Shen^{b,c,*}

^a*School of Information and Technology, Northwest University, Xi'an, China*

^b*Department of Radiology and Biomedical Research Imaging Center (BRIC), University of North Carolina at Chapel Hill, NC, U.S.A.*

^c*Department of Brain and Cognitive Engineering, Korea University, Seoul, Korea*

ARTICLE INFO

Keywords:

Denoising Filter
Adaptive Filtering
Bilateral Filtering
Gestalt Grouping Rules
Hierarchically Clustering
Simulation of Vision Adaptivity

ABSTRACT

Bilateral filtering is one of the most classical denoising filters. However, the parameter of its range kernel needs to be initialized manually, which hampers its adaptivity across images with different characteristics. For coping with image variation (e.g., changeable signal-to-noise ratio and spatially-varying noise), it is necessary to adapt the kernel to specific image characteristics automatically. In this paper, we propose multi-kernel filter (MKF) inspired by adaptive mechanisms of human vision. We first design a hierarchically clustering algorithm to generate a hierarchy of large to small coherent image patches, organized as a cluster tree, so that multi-scale represent an image. One leaf cluster and two corresponding predecessor clusters are used to generate one of a number of range kernels that are capable of catering to image variation. We evaluate MKF on two public datasets, BSD300 and Phantomas. Extensive experimental results show that MKF outperforms various state-of-the-art filters on both mean absolute error and structural similarity.

1. Introduction

Image filtering is a crucial preprocessing approach, which serves widely in practical tasks, including noise removal (Veraart, Novikov, Christiaens, Ades-Aron, Sijbers and Fieremans, 2016b), edge detection (Wei, Yang and Gong, 2018), and phase correction (Eichner, Cauley, Cohen-Adad, Möller, Turner, Setsompop and Wald, 2015). To customize a filter for one task, it needs to optimize filtering parameters manually. As a result of this, the filter only performs optimally on images with expected characteristics. However, if image characteristics deviate the expectation, the filtering performance would degenerate because the fixed parameters cannot cater to image variation. In practice, it can be challenging for applying such a filter on images with variabilities (e.g., changeable signal-to-noise ratio (SNR) and spatially-varying noise).

While it needs to manually initialize parameters of conventional filters, the most popular convolution neural networks integrate a mass of learnable convolutional filters (LeCun, Bottou, Bengio, Haffner et al., 1998; Bruna, Zaremba, Szlam and Lecun, 2014; Monti, Boscaini, Masci, Rodola, Svoboda and Bronstein, 2017). Those filters can tolerate image variation within the training dataset, but they are considered as task- and dataset-dependent. If an image varies significantly, unexpected characteristics will degenerate those learned filters as well.

Bilateral filtering (BF) (Tomasi and Manduchi, 1998) is one of the most classical filters. It makes full use of image redundancy, namely, uncorrupted pixels. To measure redundancy, the range kernel in BF employs a Gaussian kernel. The standard deviation in the kernel determines a fixed intensity range at each pixel. Neighbor pixels which intensity is in the range are considered as redundant and are used to generate the weighted mean so that BF distinguishes the noise from edges. This filtering strategy performs optimally when the noise level is constant and when the edge gradient is larger than the noise level. However, this assumption is unpractical.

By contrast, the human vision system adapts to circumstances and selectively neglects uninterested objects (Bar, 2004; Parr and Friston, 2019), without relying on a fixed filtering policy. A circumstance, on the negative side, may

[★]This work was supported in part by the National Key Research and Development Program of China under grant (2017YFB1002504), and by NIH grants (NS093842 and EB022880).

The authors have declared that no competing interests exist.

*Corresponding authors

 child@stumail.nwu.edu.cn (F. Liu); fengjun@nwu.edu.cn (J. Feng); ptyap@med.unc.edu (P. Yap); dgshen@med.unc.edu (D. Shen)

ORCID(s): 0000-0001-5199-5261 (F. Liu)

induce visual illusion. The same physical appearance can be recognized as different identities, e.g., the illusion in low-level vision (*Checker Shadow*) and high-level vision (*Rabbit-duck*). On the positive side, it allows a human to adapt to varying environments efficiently (Bar, 2004; Lu, Yin, Chen, Gong, Liu, Qian, Li, Liu, Andolina and Wang, 2018). Theoretically, such adaptive mechanisms may rely on visual working memory (Gao, Gao, Li, Sun and Shen, 2011; Eriksson, Vogel, Lansner, Bergström and Nyberg, 2015; Thiele and Bellgrove, 2018), where obeys Gestalt grouping rules in forming visual objects (Peterson and Berryhill, 2013; Gao, Gao, Tang, Shui and Shen, 2016).

Inspired by the robust human vision, in this paper, we propose multi-kernel filter (MKF) for improving adaptivity of range kernel in BF. We first design a hierarchically clustering algorithm, following Gestalt grouping rules, so that obtain a hierarchy of large to small coherent image patches, which are organized as a cluster tree for multi-scale representing an image (Sec. 3.1). A leaf cluster of the tree is used to generate one of a number of kernels, and these kernels are further fine-tuned by corresponding predecessor clusters (Sec. 3.2). Predecessor clusters serve as the circumstance or *image context* where the leaf cluster is in, providing additional constraints. After our extension, the single spatially-invariant range kernel in BF, now, becomes multiple spatially-varying ones. Most importantly, their parameters become to be automatically determined by the image content itself, rather by manual. We will demonstrate with extensive experimental results that MKF achieves high-level adaptivity on images with variabilities mentioned above, outperforming BF and various state-of-the-art filters (Sec. 4).

2. Related Works

In filtering tasks, noisy pixels can be restored from redundant image regions. To detect image redundancy, the estimation on edge gradient, noise level, or intensity distribution, is beneficial to bring additional constraints since image filtering is widely believed as an ill-posed problem. Early on, for avoiding blurring edges, the mean filter is improved through measuring intensity variation in local; only pixels within a rectangular window that has the smallest intensity variance are used to generate the mean (Nagao and Matsuyama, 1979).

Afterward, to avoid smoothing across edges that are boundaries of a coherent image region, a spatially-invariant weight matrix is employed to detect and extract edges (Burt, 1981). However, it still blurs edges. The anisotropic diffusion filter employs a Gaussian kernel to precisely detect edges, but it is low in time efficiency (Perona and Malik, 1990). To overcome such limitations, BF generates spatially-varying weight matrixes at each pixel using an extended spatially-invariant Gaussian kernel (Tomasi and Manduchi, 1998). The filtering process of BF can be formulated in a generalized intensity space (Barash, 2002); from this geometric perspective, the detection of edges can be interpreted as measuring the distance between pixels.

Compared with the prior knowledge of noise level or edge gradient, the piece-wise constant intensity distribution can be naturally considered as another sign of image redundancy. Image denoising can be achieved by suppressing the intensity variation. Total Variation (TV) targets this goal through minimizing a global cost (Rudin, Osher and Fatemi, 1992), which is weighed by a regularization parameter that trades between the fidelity and smoothness terms. TV does not need to estimate the noise level and thus is commonly used to cope with spatially-varying noise (Eichner et al., 2015; Pizzolato, Fick, Boutilier and Deriche, 2016). And next, Curvature Filter (CF) extends TV allowing more geometric configurations in local (Gong and Sbalzarini, 2017). Although the regularization parameter exerts a function akin to controlling the SNR of the filtered image, how to initialize it is not intuitive.

More than that, the accurate detection on noise level is also beneficial. Because the noise can be modeled by a random matrix which eigenvalues obey universal Marchenko-Pastur distribution (Veraart, Fieremans and Novikov, 2016a), it can precisely identify the noise using corresponding principal components. Thus, with the estimated noise levels, Marchenko-Pastur PCA (MPPCA), is designed for 4D diffusion MRI (DMRI) data for appropriately coping with the spatially-varying noise (Veraart et al., 2016b).

3. The Proposed Method

To improve the adaptivity of range kernel in BF, we first propose a hierarchically clustering algorithm for multi-scale representing an image (Sec. 3.1); and then, we reinterpret BF from a geometric view and demonstrate a promising attempt for automatically specifying the parameters (Sec. 3.2).

3.1. A Hierarchically Clustering Algorithm for Image Context Construction

We design the hierarchically clustering algorithm taking the inspiration from human vision system. A human adaptively perceives visual information taking advantage of a context, which does not only comprise of visual objects

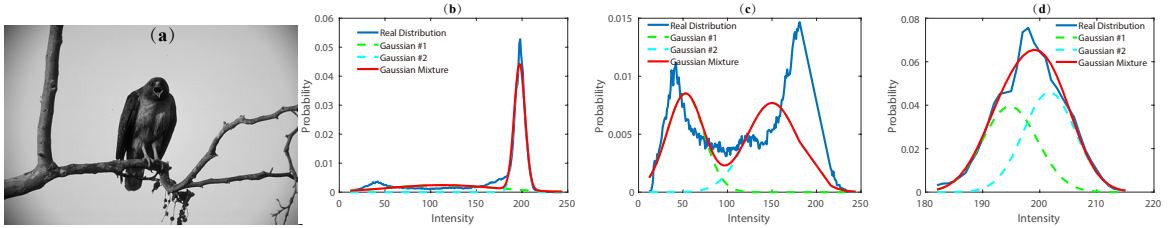


Figure 1: Two rounds of similarity clustering. (a) An eagle image selected from BSD300. (b) After the first round, all pixels are aggregated into two groups which intensity distributions are modeled by #1 and #2 Gaussian distributions respectively (marked by dash-curves). Solid blue curves in (c) and (d) show exact intensity distributions of the two groups, respectively. The solid red curves denote the mixture of two Gaussian models. We can find the red curves in (c) and (d) fit the intensity distribution more closely than it in (b).

but also their associations (Bar, 2004). More specifically, the principles of perceptual object formation can be depicted by Gestalt grouping rules (i.e., similarity and proximity rules) (Gao et al., 2011; Wagemans, Elder, Kubovy, Palmer, Peterson, Singh and von der Heydt, 2012; Peterson and Berryhill, 2013; Gao et al., 2016). Following such rules, we design the clustering to obtain a hierarchy of large to small coherent image patches for simulating the visual objects and their associations. The obtained clusters are organized by a cluster tree so that easily extract the contextual information of a specific image region.

3.1.1. Two-Stage Clustering for Hierarchical Image Representation

Following the top-down paradigm, the hierarchically clustering targets to recursively aggregate pixels into large to small coherent image patches. Two objectives of the clustering algorithm are (1) to simulate similarity and proximity Gestalt grouping rules, and (2) to adaptive generate the total number of clusters.

To achieve the first objective, each round of the clustering comprises two stages: (i) intensity based *similarity clustering*, and (ii) connectedness based *proximity clustering*. At first, similarity clustering employs expectation maximization (EM) for 'soft' aggregating similar pixels; and then, proximity clustering further partitions the outcome of similarity-clustering into spatially connected ones.

In the first stage, *similarity clustering* dissects the input pixels $\{I(\vec{x}_1) \dots I(\vec{x}_m) \dots I(\vec{x}_n)\}$ into two coherent groups with labels $\{\ell_1, \ell_2\}$. The intensity distribution of both groups can be modeled by two Gaussian models respectively, which parameters are learned by the maximum log-likelihood method, given by,

$$\arg \max_{\theta_{t,k}^*} \sum_{\ell \in \{\ell_1, \ell_2\}} p(\ell | I(\vec{x}_m), \theta_{t,k}) \log p(I(\vec{x}_m), \ell | \theta_{t,k}^*), \quad (1)$$

where $\theta_{t,k} = \{\mu_{t,k}, \delta_{t,k}\}$ is a parameter set consisting of mean $\mu_{t,k}$ and standard deviation $\delta_{t,k}$ of the k -th cluster at the t -th layer.

Figure 1 shows the Gaussian distributions, learned from two rounds of similarity clustering, which represent the image in two scales. As shown in Figure 1(b), after the first round of similarity clustering, the input pixels are partitioned into two groups which are represented by two Gaussian distributions in coarse-scale. Based on the coarse result, fine-scale Gaussian distributions are generated by the second round of clustering, shown in Figure 1(c) and 1(d) respectively. For illustrating representation precision of such two rounds of similarity clustering, the result label maps are shown in Figure 2.

In the second stage, *proximity clustering* isolates unconnected pixels, generating a total of n_t clusters at the t -th layer, and the image I can be represented by Gaussian mixture model (GMM), G_t , given by,

$$G_t = \sum_{k=1}^{n_t} \mathcal{N}(\mu_{t,k}, \delta_{t,k}), \quad (2)$$

As t increases, the number of clusters increases accordingly. Thus, the intensity variation of each cluster decreases, and G_t precisely represents the image.

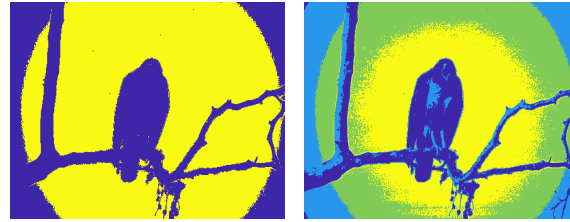


Figure 2: Label maps of two rounds of similarity clustering. It first splits the input pixels into 2 groups (left), and then, 4 groups (right). The label map in right is more similar to the original image and shows more details than the left one.

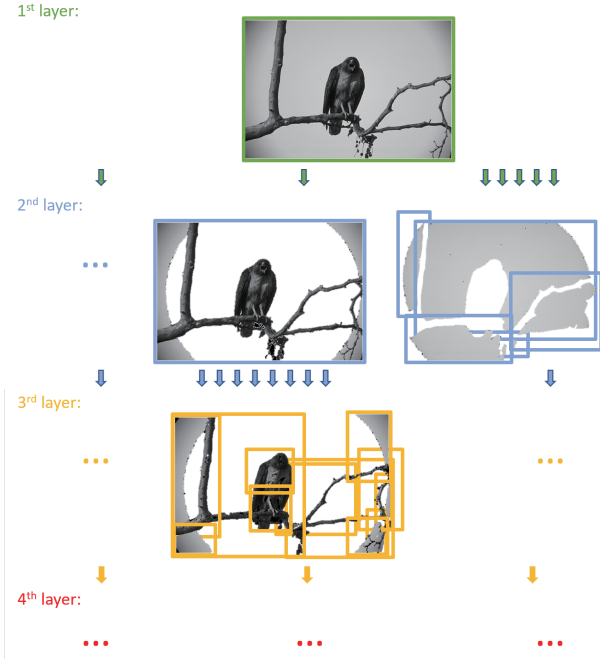


Figure 3: Partial branches of a cluster tree. Each bounding box denotes a node (i.e., cluster). As the tree depth increases, the intensity variation of a leaf cluster decreases accordingly. We can see a cluster in 2nd layer contains high-contrast contents, such as the whole eagle; while a cluster in 3rd layer only contains one leg which shows low-contrast. We specify the clusters in upper layers as image context of corresponding leaf cluster.

3.1.2. Image Context Represented by Cluster Tree

In human vision system, low-resolution signals provide contextual cues (Bar, 2004; Peterson and Berryhill, 2013; Lu et al., 2018). Inspired by this, we construct the cluster tree, in which a predecessor cluster is specified as the image context of its corresponding leaf clusters. More specifically, a cluster in the leaf layer associates with predecessor clusters in upper layers. To vividly illustrate such affiliation, one exemplary cluster tree is shown in Figure 3. Layers in the cluster tree, from root to leaf, represent the image, from coarse to fine.

To construct the cluster tree, MKF should initialize two parameters, i.e., maximal cluster size and maximal tree depth. The clustering will be terminated if the input pixel number is less than maximal cluster size, or if the cluster tree reaches maximal tree depth. Both parameters heuristically determine the total number of clusters in the leaf layer so that obtain coherent image patches that can suit for various images. By this, we heuristically obtain the total cluster number and achieve the second objective mentioned at the beginning of last subsection.

To here, we are clear about how to generate the cluster tree for constructing image context. For denoising, those learned deviations in the leaf layer are exploited to automatically generate spatially-varying kernels, while the upper ones bring contextual constraintWW to refine such kernels.

3.2. Multi-Kernel Filter (MKF) for Image Denoising

3.2.1. Reinterpretation of BF

BF distinguishes edges or noises relying on the manually specified parameter of range kernel. Employing a spatially-invariant Gaussian kernel, the range kernel detects receivable neighbor pixels and computes their weighted mean to replace the intensity of central pixel. This filtering process can be analyzed in a generalized intensity space (Barash, 2002), given by,

$$\hat{I}(\vec{x}) = \left\{ \frac{I(\vec{x})}{h_I}, \frac{\vec{x}}{h_{\vec{x}}} \right\}, \quad (3)$$

where $h_{\vec{x}}$ is the constant conduction coefficient in spatial, and h_I is the parameter of range kernel. Both are manually initialized. After several steps of derivation, bilateral filtering can be rewritten by,

$$O(I(\vec{x})) = I(\vec{x}) + R\left(\hat{I}(\vec{x}), \hat{I}(\vec{\xi})\right), \quad (4)$$

where $\vec{\xi}$ denotes the coordinate of neighbor pixels centered at \vec{x} , and $R\left(\hat{I}(\vec{x}), \hat{I}(\vec{\xi})\right)$ is given by,

$$R\left(\hat{I}(\vec{x}), \hat{I}(\vec{\xi})\right) = \frac{\sum_{\vec{\xi}} \hat{w}(\vec{x}, \vec{\xi}) (I(\vec{\xi}) - I(\vec{x}))}{\sum_{\vec{\xi}} \hat{w}(\vec{x}, \vec{\xi})}, \quad (5)$$

where $(I(\vec{\xi}) - I(\vec{x}))$ is intensity difference between neighbor pixels, and the kernel can be written by $\hat{w}(\vec{x}, \vec{\xi}) = \exp\left\{-\frac{1}{2} \|\hat{I}(\vec{x}) - \hat{I}(\vec{\xi})\|^2\right\}$ in the generalized space. As the weights of pixels are normalized, $R\left(\hat{I}(\vec{x}), \hat{I}(\vec{\xi})\right)$ can be interpreted as the expectation of local intensity variation, which measures local smoothness when considering an image as a 2D manifold embedded in a 3D Euclidean space. Since a fixed kernel cannot cater to image variation, we hence improve it using the cluster tree.

3.2.2. Adaptive Filtering of MKF

To cater to image variation, we reformulate edge-discernment taking advantage of contextual information. Each leaf node of the tree is utilized to generate one of a number of kernels, and next, these kernels are fine-tuned by corresponding predecessor nodes. Contrasting the manually specified parameter in BF, the edge-discernment now depends on the parameters learned.

MKF is formulated by,

$$O(I(\vec{x})) = I(\vec{x}) + R\left(\hat{I}(\vec{x}), \hat{I}(\vec{\xi}) \mid \delta_{t,k}, \Psi_{t,k}\right), \quad (6)$$

where the extended $R(\cdot)$, estimating the expectation of local intensity variation, is now dependent on $\delta_{t,k}$, which encodes local information, and $\Psi_{t,k}$, which takes into consideration contextual information. The kernel employed in $R(\cdot)$ is given by,

$$w(\vec{x}, \vec{\xi} \mid \delta_{t,k}, \Psi_{t,k}) = \exp \left\{ \frac{-(\vec{x} - \vec{\xi})^2}{2h_{\vec{x}}^2} + \frac{-\Delta I^2(\vec{x}, \vec{\xi})\Psi_{t,k}}{2\delta_{t,k}^2} \right\}, \quad (7)$$

where $\Delta I(\vec{x}, \vec{\xi}) = (I(\vec{\xi}) - I(\vec{x}))$ denotes intensity difference, and $\Psi_{t,k}$ is given by,

$$\Psi_{t,k} = \left(\frac{\delta_{t-1,k^*}}{\delta_{t-2,k^{**}}} \right)^2, \quad (8)$$

where k^* and k^{**} denote corresponding labels of k in $(t-1)$ - and $(t-2)$ -th layers respectively. Both $\delta_{t,k}$ and $\Psi_{t,k}$ allow the same $\Delta I(\vec{x}, \vec{\xi})$ to generate different weights. Meanwhile, $\Psi_{t,k}$ also exerts a function on $\delta_{t,k}$. The same

local variation level may have different implications according to different contextual information. Typically, $\delta_{t-2,k^{**}} > \delta_{t-1,k^*}$, therefore, $\Psi_{t,k} < 1$, which enlarges $\delta_{t,k}$.

The filtering strategy of MKF is akin to the selective filtering mechanisms of human vision system, i.e., the salient object drives human to neglect non-salient objects involuntarily. In MKF, high image contrast is considered as salient, inducing the filtering kernels to filter out low contrast image contents.

More specifically, the contextual information of a leaf cluster, $C_{t,k}$, is provided by its predecessor cluster, such as C_{t-1,k^*} and $C_{t-2,k^{**}}$, which surround $C_{t,k}$. The $\Psi_{t,k}$ encodes the contrast information of the surrounding image regions. A $\Psi_{t,k}$ close to 0 demonstrates large contrast, which significantly enlarges $\delta_{t,k}$ so that MKF smooths across the boundaries of $C_{t,k}$. Therefore, lower contrast contents represented by $C_{t,k}$ are smoothed out, no matter $C_{t,k}$ represents a small object or noise. Otherwise, when $\Psi_{t,k}$ is close to 1, it denotes low-contrast of surrounding image regions. Thus, $\Psi_{t,k}$ slightly enlarges $\delta_{t,k}$ for intraregional smoothing so that reserves the boundaries of $C_{t,k}$.

Incorporating $\delta_{t,k}$ and $\Psi_{t,k}$ into the range kernel, MKF can adaptively determines what contents should be filtered out only considering the image content itself. This enables MKF to cater to image variabilities mentioned at the start of this manuscript.

4. Experimental Results

We evaluate MKF on two public datasets, BSD300 (Martin, Fowlkes, Tal and Malik, 2001) and *Phantomas* (Caruyer, Daducci, Descoteaux, Houde, Thiran and Verma, 2014), compared with state-of-the-art filters, including BF (Tomasi and Manduchi, 1998), weighted TV (wTV) (Pizzolato and Deriche, 2018), TV (Rudin et al., 1992), CF (Gong and Sbalzarini, 2017), and MPPCA (Veraart et al., 2016b).

4.1. Experimental Setting

BSD300: Considering the nonlinearity of the chromaticity models, we convert the 100 test color images to grayscale. All images are separately added 100 levels of Gaussian noise, which level is from 10 to 1000 with an interval of 10. The noise level can be normalized by dividing 65025 (255 × 255) according to the range of **UINT8**.

Phantomas: To generate synthetic DMRI data, we employ imaging parameters: $b = 750, 1500, 3000$ s/mm²; a total of 64 gradient directions; including b_0 , the data had 4 b -values; image size=110 × 110. In other words, plus 5 b_0 volumes, the synthetic data had 69 3D volumes, each of which comprise 110 images with size 110 × 110. As the large b -value attenuates image signals, the SNR of DMRI images decreases with signal attenuation. Contrasting with the case that image SNR changes with integrally varying noise in Sec. 4.2, the noise levels in DMRI images is spatially-varying (Aja-Fernández, Pie, Vegas-Sánchez-Ferrero et al., 2015; Chen, Dong, Zhang, Lin, Shen and Yap, 2019a).

We fix well-chosen parameters of filters for observing filtering adaptivity. To show the improvement, MKF is compared with BF on BSD300 employing the mean absolute error (MAE) and structural similarity (SSIM) indices. Filters, including TV, CF, MPPCA (a promising 4D denoising filter), and wTV (a design for resolving the spatially-varying noise issue in DMRI), are evaluated on *Phantomas*.

4.2. Adaptivity under Integrally Varying Noise

We first quantitatively evaluate how parameters (i.e., cluster size and tree depth) of the clustering affect the smoothing performance of MKF in respect to MAE and SSIM. A small MAE value accompanying a large SSIM value demonstrates high-quality denoising performance.

We choose the #33039 image that is separately added 10 and 1000 two levels of noise. To initialize MKF, the tree depth t is chosen from 2 to 7, and the cluster size is from 10 to 200 with an interval of 10. Typically, $\Psi_{t,k} = (\delta_{t,k}/\delta_{t-1,k^*})^2$ when $t = 2$.

As shown in Figure 4.2, tree depth demonstrates a contrary effect. When $t = 7$, MKF achieves the best performance under small level noise while achieving the worst performance under severe noise. We can find from Figure 4.2, when $t = 2$, the MAE and SSIM curves are more flat no matter under the noise level of 10 or 1000. Typically, MKF performs slightly better when the cluster size turns 10.

The contrary effect of tree depth largely owes to the clustering. First of all, the tree depth indirectly affects the cluster size. A large t makes clusters in the leaf layer be small, while a small t generates large ones. Second, small clusters represent the image in fine-scale, and hereby, allow MKF to precisely reserve the detailed image contents.

MKF: An extension of BF using image context

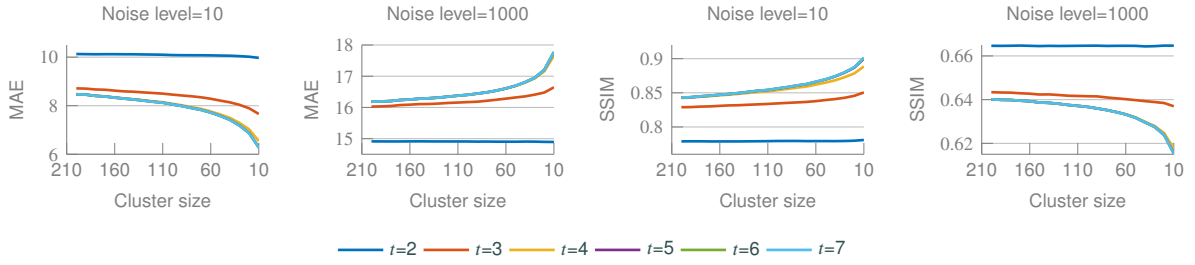


Figure 4: A negative correlation between the tree depth and noise level. While a large tree depth performs better on the image with small-level noise, a small tree depth is beneficial to restore image from severe noise.

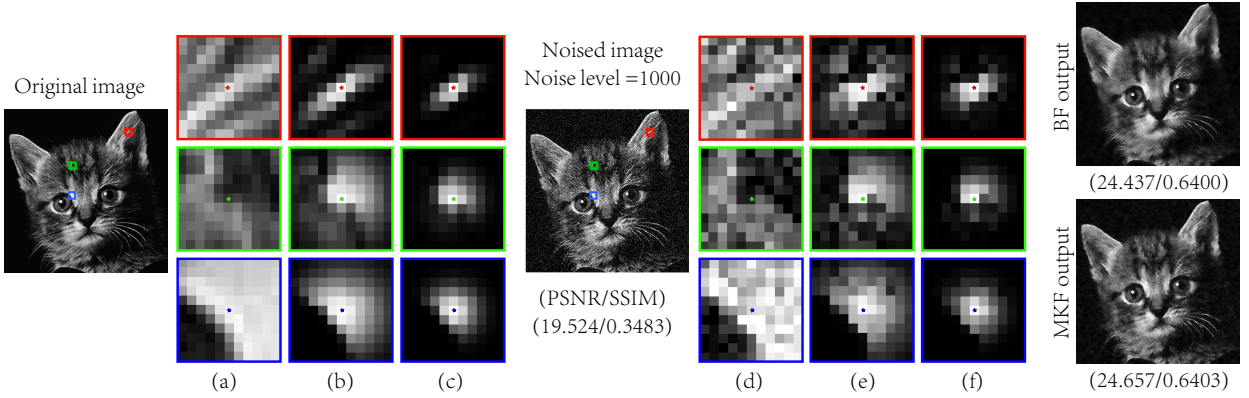


Figure 5: Severe noise (1000) significantly corrupts image contents as well as the filtering kernel. Three typical noise-free and noisy image patches, shown in (a) and (d) respectively, are used to demonstrate such degeneration. The filtering kernels of BF are shown in (b) and (e); while (c) and (f) denote MKF. Due to a local image region is easily corrupted, BF kernels degenerate apparently. Using contextual information, MKF is more robust, allowing to restore more textures and show better quantitative performance than BF.

On the contrary, severe noise corrupts image details significantly. Thus, the statistic in a small image region is not reliable, and a large image region is preferred owing to more redundant pixels.

Using the cat image (Tomasi and Manduchi, 1998; Barash, 2002), which contains both flat and texture regions, we first evaluate the weight matrixes derived by BF and MKF respectively. The h_I of BF is initialized as 57, which is the best one; h_x is 3, and window radius is 5. In MKF, we specify the tree depth 2, cluster size 20, and other parameters are the same with BF.

The weight matrixes obtained from noise-free and severely noised images are shown in Figure 5. The weight matrixes of BF are severely corrupted, resulting in an oversmoothed cat with blurred contents shown in Figure 5. In the meanwhile, MKF not only demonstrates more robust filtering kernels but also restores a cat with more detailed textures than BF.

To observe the adaptivity under a series of integrally varying noises over various images, we further evaluate MKF and BF on BSD300 under two sets of parameters. For MKF, (i) tree depth $t = 2$, cluster size 20; and (ii) tree depth $t = 7$, cluster size 20. As for BF, (i) $h_I = 57$; and (ii) $h_I = 5$. Other parameters are the same with above experiment. As shown in Figure 6, different parameters of BF affected its performance more apparently. Typically, BF shows a non-linear relationship between noise level and the MAE and SSIM performance, while MKF demonstrates a near linear correlation when $t = 2$. Besides improving the noise removal capacity, above experiments support that MKF achieves a higher-level of adaptivity than BF.

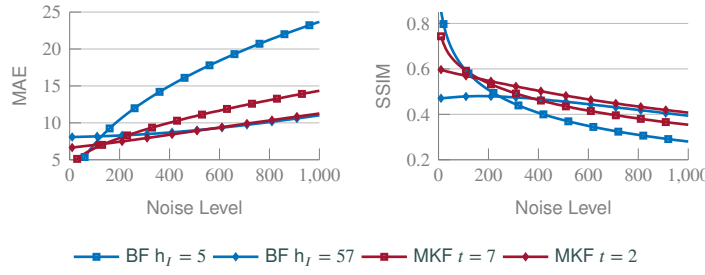


Figure 6: Due to the parameter learning, MKF adapts to image variation better than BF, demonstrating the robustness of MKF.

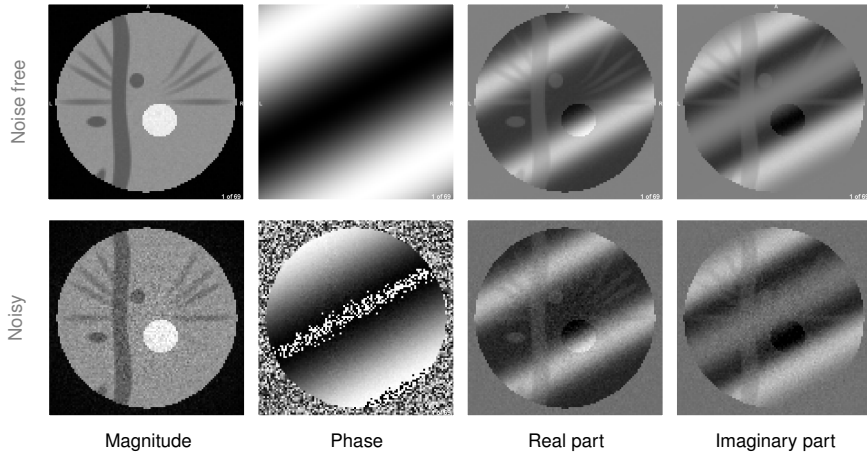


Figure 7: Synthetic DMRI data. Noise-free and noisy synthetic data of a b_0 slice.

4.3. Adaptivity under Spatially-Varying Noise

On phantoms, we still employ the same parameters of BF and MKF except of the window radius, which now is 1 considering the image size turns to much smaller. For evaluation, we compare MKF with BF, MPPCA, CF, TV, and wTV. Their parameters are well chosen and are listed as following. The maximal iteration of TV is 10 and the λ was 2. In MPPCA, we set a block size to $5 \times 5 \times 5$ recommended by Veraart et al. (2016b) for precisely estimating noise levels. We choose the Gaussian curvature in CF and set the maximal iteration 10. wTV is initialized with the same parameters of TV but with an additional window size 15×15 recommended by Pizzolato and Deriche (2018) for estimating noise levels.

Under the background of phase correction (Eichner et al., 2015), a filter is employed to smooth both complex components of DMRI data. To derive noise-free real and imaginary components, we synthesize the background phase according to Pizzolato et al. (2016). The intensity range of both components is roughly from -9000 to 9000 . We next add the spatially varying noise with a maximal level of 2000 according to Chen, Wu, Shen and Yap (2019b). It should point out that the phase maps are slice-by-slice varying and were gradually transitional; typically, this breaks the low-rank assumption of an image. We can see the noise free and noisy synthetic data for a b_0 slice in Figure 7.

Figure 8 shows 4 noise-free (last column) and noisy slices (first column) with 4 b -values, which show the denoised images of 6 filters. From the top row to bottom, b -values are ordered ascendingly and the SNR turns small. We can see in Figure 8, the noise severely corrupts detailed image contents. After denoising, however, BF still reserves a lot of noise points; wTV removes noise only in part of image regions. Although TV and CF achieve better results, they demonstrate mosaic blocks; and MPPCA and MKF generate smoother results which are close to the noise-free ground truth. For more pieces of qualitative evidence, we further derive their residual noise maps.

The residual noise maps are obtained by subtracting the smoothed image from its noisy counterpart. The residual map should better only contain Gaussian noise, indicating the filter has achieved an ideal smoothing capacity. BF generates near blank maps, shown in Figure 9, because the fixed parameter cannot adapt to the changed noise level.

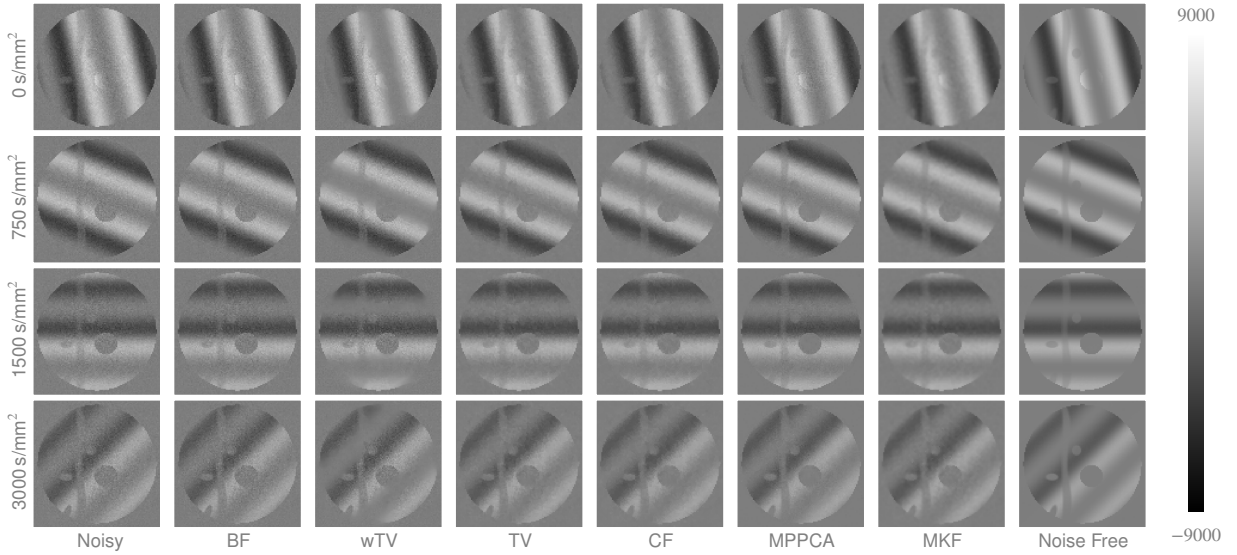


Figure 8: Four imaginary slices with $b = 0, 750, 1500, 3000 \text{ s/mm}^2$ demonstrate the promising denoising performance of MKF.

Except wTV, other filters obtain noise maps with less textures, but TV and CF show more textures than MPPCA and MKF. To quantitatively demonstrate the effectivity of MKF, we further evaluate their MAE and SSIM indices.

In Figure 4.3, MAE and SSIM curves illustrate the quantitative indices. The curves demonstrate the mean MAE and SSIM values derived by 110 image of one volume. MKF achieves a better MAE and SSIM performance than BF, wTV, TV, and CF and shows competitive performance compared with MPPCA. Moreover, the MAE curves of MKF no matter in real or imaginary components are flatter than other filters', indicating it is affected by b -values the least. Those results support a prominent improvement achieved by MKF.

5. Discussion and Conclusion

To improve filtering adaptivity, we extended the range kernel of bilateral filtering using the image context. The image context was novelly constructed through the proposed clustering method, which follows Gestalt grouping rules, so that the range kernel can be automatically initialized by the image content itself. With this extension, MKF demonstrates a higher-level adaptivity than BF, and shows promising noise-removal performance even outperforming various state-of-the-art filters. As far as we know, this is the first study investigating and simulating the adaptive visual mechanisms in designing a smoothing filter. However, some limitations are worth noting. Although MKF adaptively generates parameters of filtering kernels, its performance depends on the parameters of the clustering, and MKF is relatively low in time efficiency owing to the hierarchically clustering. Future works should develop a more effective computational model of vision adaptivity for addressing such limitations.

References

Aja-Fernández, S., Pie, T., Vegas-Sánchez-Ferrero, G., et al., 2015. Spatially variant noise estimation in MRI: A homomorphic approach. *Medical Image Analysis (MIA)* 20, 184–197.

Bar, M., 2004. Visual objects in context. *Nature Reviews Neuroscience* 5, 617–629.

Barash, D., 2002. Fundamental relationship between bilateral filtering, adaptive smoothing, and the nonlinear diffusion equation. *IEEE Transactions on Pattern Analysis and Machine Intelligence (TPAMI)* 24, 844–847.

Bruna, J., Zaremba, W., Szlam, A., Lecun, Y., 2014. Spectral networks and locally connected networks on graphs, in: *International Conference on Learning Representations (ICLR)*.

Burt, P.J., 1981. Fast filter transform for image processing. *Computer Graphics and Image Processing* 16, 20–51.

Caruyer, E., Daducci, A., Descoteaux, M., Houde, J.C., Thiran, J.P., Verma, R., 2014. Phantomas: A flexible software library to simulate diffusion MR phantoms, in: *23rd annual meeting of the International Society for Magnetic Resonance in Medicine (ISMRM)*.

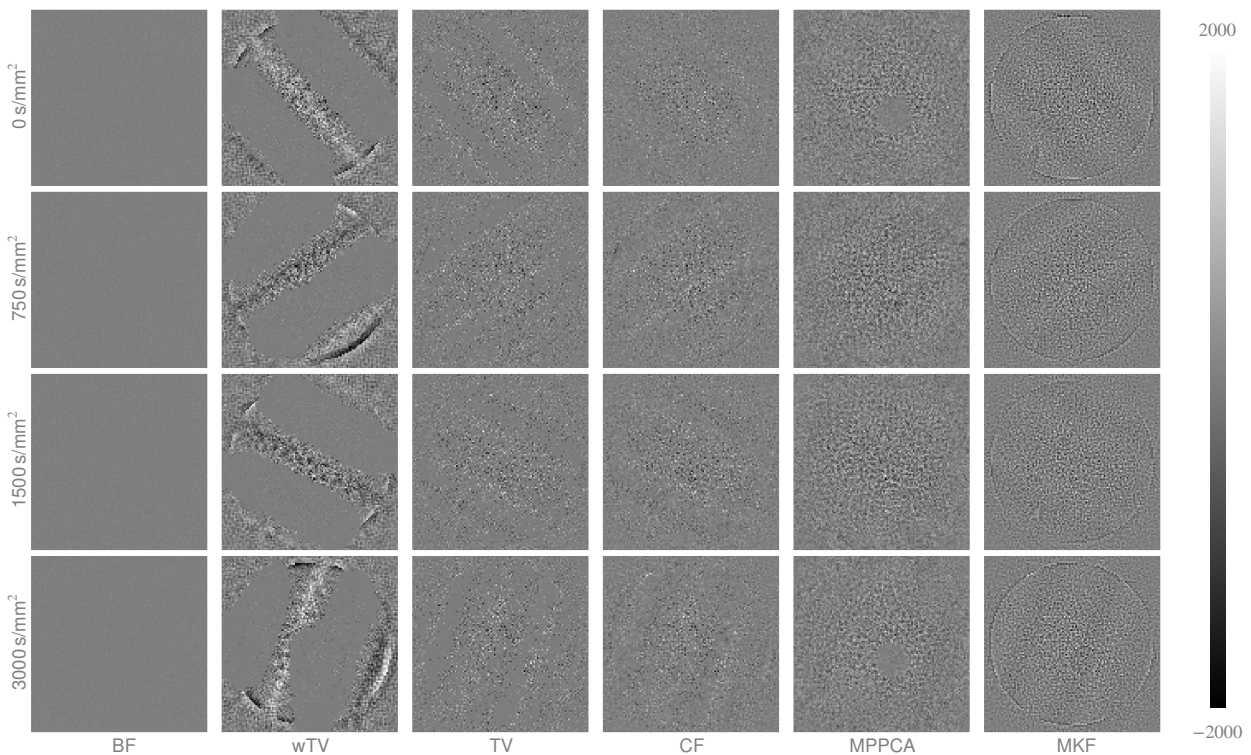


Figure 9: Four residual noise maps of the imaginary components with $b = 0, 750, 1500, 3000 \text{ s/mm}^2$. BF and wTV show apparent blank regions which indicates ineffective noise-removal. TV and CF are better, but less than MPPCA. Fewer textures derived by MPPCA and MKF demonstrate better performance.

Chen, G., Dong, B., Zhang, Y., Lin, W., Shen, D., Yap, P.T., 2019a. Denoising of infant diffusion MRI data via graph framelet matching in x - q space. *IEEE Transactions on Medical Imaging (TMI)*.

Chen, G., Wu, Y., Shen, D., Yap, P.T., 2019b. Noise reduction in diffusion MRI using non-local self-similar information in joint x - q space. *Medical Image Analysis (MIA)* 53, 79–94.

Eichner, C., Cauley, S.F., Cohen-Adad, J., Möller, H.E., Turner, R., Setsompop, K., Wald, L.L., 2015. Real diffusion-weighted MRI enabling true signal averaging and increased diffusion contrast. *NeuroImage* 122, 373–384.

Eriksson, J., Vogel, E.K., Lansner, A., Bergström, F., Nyberg, L., 2015. Neurocognitive architecture of working memory. *Neuron* 88, 33–46.

Gao, T., Gao, Z., Li, J., Sun, Z., Shen, M., 2011. The perceptual root of object-based storage: An interactive model of perception and visual working memory. *Journal of Experimental Psychology: Human Perception and Performance* 37, 1803–1823.

Gao, Z., Gao, Q., Tang, N., Shui, R., Shen, M., 2016. Organization principles in visual working memory: Evidence from sequential stimulus display. *Cognition* 146, 277–288.

Gong, Y., Sbalzarini, I.F., 2017. Curvature filters efficiently reduce certain variational energies. *IEEE Transactions on Image Processing (TIP)* 26, 1786–1798.

LeCun, Y., Bottou, L., Bengio, Y., Haffner, P., et al., 1998. Gradient-based learning applied to document recognition. *Proceedings of the IEEE* 86, 2278–2324.

Lu, Y., Yin, J., Chen, Z., Gong, H., Liu, Y., Qian, L., Li, X., Liu, R., Andolina, I.M., Wang, W., 2018. Revealing detail along the visual hierarchy: Neural clustering preserves acuity from V1 to V4. *Neuron* 98, 417–428.

Martin, D., Fowlkes, C., Tal, D., Malik, J., 2001. A database of human segmented natural images and its application to evaluating segmentation algorithms and measuring ecological statistics, in: *Proceedings of the IEEE International Conference on Computer Vision (ICCV)*, pp. 416–423.

Monti, F., Boscaini, D., Masci, J., Rodola, E., Svoboda, J., Bronstein, M.M., 2017. Geometric deep learning on graphs and manifolds using mixture model CNNs, in: *Proceedings of the IEEE Conference on Computer Vision and Pattern Recognition (CVPR)*, pp. 5115–5124.

Nagao, M., Matsuyama, T., 1979. Edge preserving smoothing. *Computer Graphics and Image Processing* 9, 394–407.

Parr, T., Friston, K.J., 2019. Attention or salience? *Current Opinion in Psychology* 29, 1–5.

Perona, P., Malik, J., 1990. Scale-space and edge detection using anisotropic diffusion. *IEEE Transactions on Pattern Analysis and Machine Intelligence (TPAMI)* 12, 629–639.

Peterson, D.J., Berryhill, M.E., 2013. The Gestalt principle of similarity benefits visual working memory. *Psychonomic Bulletin & Review* 20,

MKF: An extension of BF using image context

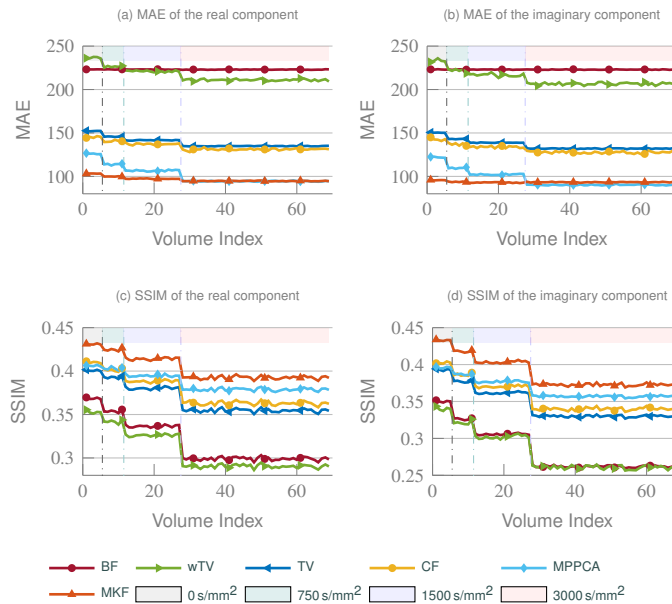


Figure 10: MKF achieves better MAE and SSIM indices than BF, wTV, TV, and CF, and is competitive to MPPCA.

1282–1289.

Pizzolato, M., Deriche, R., 2018. Automatic and spatially varying phase correction for diffusion weighted images, in: 26th annual meeting of the International Society for Magnetic Resonance in Medicine (ISMRM).

Pizzolato, M., Fick, R., Boutelier, T., Deriche, R., 2016. Noise floor removal via phase correction of complex diffusion-weighted images: Influence on DTI and Q-space metrics, in: MICCAI Workshop on Computational Diffusion MRI, pp. 21–34.

Rudin, L.I., Osher, S., Fatemi, E., 1992. Nonlinear total variation based noise removal algorithms. **Physica D: Nonlinear Phenomena** 60, 259–268.

Thiele, A., Bellgrove, M.A., 2018. Neuromodulation of attention. **Neuron** 97, 769–785.

Tomasi, C., Manduchi, R., 1998. Bilateral filtering for gray and color images, in: Proceedings of the IEEE International Conference on Computer Vision (ICCV), pp. 839–846.

Veraart, J., Fieremans, E., Novikov, D.S., 2016a. Diffusion MRI noise mapping using random matrix theory. **Magnetic resonance in medicine (MRM)** 76, 1582–1593.

Veraart, J., Novikov, D.S., Christiaens, D., Ades-Aron, B., Sijbers, J., Fieremans, E., 2016b. Denoising of diffusion MRI using random matrix theory. **NeuroImage** 142, 394–406.

Wagemans, J., Elder, J.H., Kubovy, M., Palmer, S.E., Peterson, M.A., Singh, M., von der Heydt, R., 2012. A century of Gestalt psychology in visual perception: I. Perceptual grouping and figure–ground organization. **Psychological Bulletin** 138, 1172–1217.

Wei, X., Yang, Q., Gong, Y., 2018. Joint contour filtering. **International Journal of Computer Vision (IJCV)** 126, 1245–1265.